Axis-dependent polarity and extended van Hove singularity for exceptional transverse thermoelectricity

S. Bhagade,[1,*] M. Shahnoor Rahman,[1,*] A. Akopyan,[1] P. White,[2] J. J. Neumeier,[2] and J. L. Cohn[1,†]

[1]*Department of Physics, University of Miami, Coral Gables, FL 33124, USA*
[2]*Department of Physics, Montana State University, Bozeman, MT 59717, USA*

The conversion of a heat current into orthogonal electric current, or vice versa, offers promise for energy harvesting and heat sensing technologies. Candidate transverse thermoelectric materials for such applications possess axis-dependent conduction polarity (ADCP), i.e. Seebeck coefficients of opposite sign along mutually perpendicular crystallographic axes. Heat flow at an angle to the principal axes in such materials induces a perpendicular electric field without the need for a magnetic field as for the Nernst effect. Few ADCP materials have been identified – and fewer still with significant transverse figures of merit over an extended temperature (T) range. We report here a low-dimensional metal having transverse thermoelectric figure of merit $z_{yx}T = 0.020 - 0.05$ over the range $50 \lesssim T \lesssim 300$ K, exceeding by an order of magnitude those of anomalous Nernst materials and three or more times larger than those of other ADCP materials. The performance boost is attributed to energy-dependent scattering from an extended van Hove singularity near the Fermi energy.

Transverse thermoelectric energy conversion [1–3], where heat flow and electric current are oriented orthogonally, enables practical advantages in potential applications in comparison to the conventional longitudinal configuration, including the use of a single material, reduction in electrical contacts, and the scaling of output with size. Bulk materials possessing axis-dependent conduction polarity (ADCP) [4–8], i.e. Seebeck coefficients with opposing signs along perpendicular directions, are ideal candidates since large off-diagonal components of the thermopower tensor are generated naturally for heat or current flow at an oblique angle to the crystal axes. Though they show great promise for transverse thermoelectric applications, a scarcity of experimentally realized ADCP materials with substantial transverse thermoelectric figures of merit has limited progress.

ADCP materials have at least one of two band structure types [6] (or both): (1) two or more different bands, each of which is electron- or hole-like (the $p \times n$ or multicarrier mechanism), (2) a single band with a hyperboloidal-shaped Fermi surface that itself results in electron-like and hole-like bands in mutually perpendicular directions (so-called goniopolar materials [5]). For all ADCP materials identified thus far, the underlying mechanism is mass anisotropy for which the computed band structure predicts Seebeck coefficients along the respective crystallographic axes in good agreement with experiment. The remarkable transverse thermoelectric properties presented here for Nb_3S_4 are substantially larger than those predicted by density-functional theory and are revealed to arise from the presence of a sharp peak in the electronic density of states, associated with an extended van Hove singularity near the Fermi energy (E_F). The overlap of nearly-localized and dispersive states near E_F gives rise to substantial interband scattering that enables large Seebeck coefficients, even in metals, via effective energy filtering [9, 10]. The present observations underscore that metals possessing both ADCP *and* strong energy-dependent scattering offer a route toward practical applications.

Nb_3S_4 crystallizes in the hexagonal crystal structure with space group $P6_3/m$ [11] (Fig. 1a). NbS_6 octahedra share faces and edges forming zigzag chains (3 per unit cell) composed of Nb-Nb bonds surrounding hexagonal tunnels along the c axis. Interchain interactions are substantially reduced by intervening chalcogen atoms. The Nb_3S_4 crystals for this study (Fig. 1b) grow naturally as slightly distorted, elongated hexagonal prisms [11, 12].

Though the anisotropic electrical resistivity was reported decades ago [14], Seebeck measurements were reported only along the c axis for one specimen [15]; thermal conductivity has not been reported. A schematic illustration of the measurement setup for the two electric and heat current orientations is shown in Fig. 1c; the transport coefficients for both directions on representative crystals are shown in Fig. 1d-f; Supplementary Fig. S1 shows data for additional crystals. Notable are large residual resistivity ratios along the c axis, RRR$\sim 70-170$, indicating excellent crystalline quality. The resistive anisotropy is $\rho_\perp/\rho_\parallel \sim 5-12$. Superconductivity occurs [16–18] below $T_c \sim 4$ K (Fig. 1d). Though the Hall coefficient has not been reported to our knowledge, a highly metallic carrier density is expected, $n \gtrsim 10^{22}$ cm^{-3} (Supplementary section S1).

The ADCP character of Nb_3S_4 is reflected in the Seebeck coefficient, S (Fig. 1e) with negative (positive) sign for transport $\parallel c$ ($\perp c$). While little variation in $S_\parallel$ was observed for the crystals studied, some variability in $S_\perp$ and in the thermal conductivity κ (Fig. 1f) for both orientations was observed. This variability is likely associated with differences in the presence or density of crystal defects (e.g., intraphase intergrowths), identified in x-ray studies as multiple crystallites aligned along c with low-angle rotations of their hexagonal planes (Supplementary Figs. S2, S3).

The axial Peltier conductivities, $|\alpha| = |S|/\rho$, as functions of T for the Nb_3S_4 crystals from Fig. 1 are shown in Fig. 2a along with data for several other materials for which these coefficients are the largest known at $T < 100$ K. The measured

* These authors contributed equally to this work.
† Corresponding Author: jcohn@miami.edu

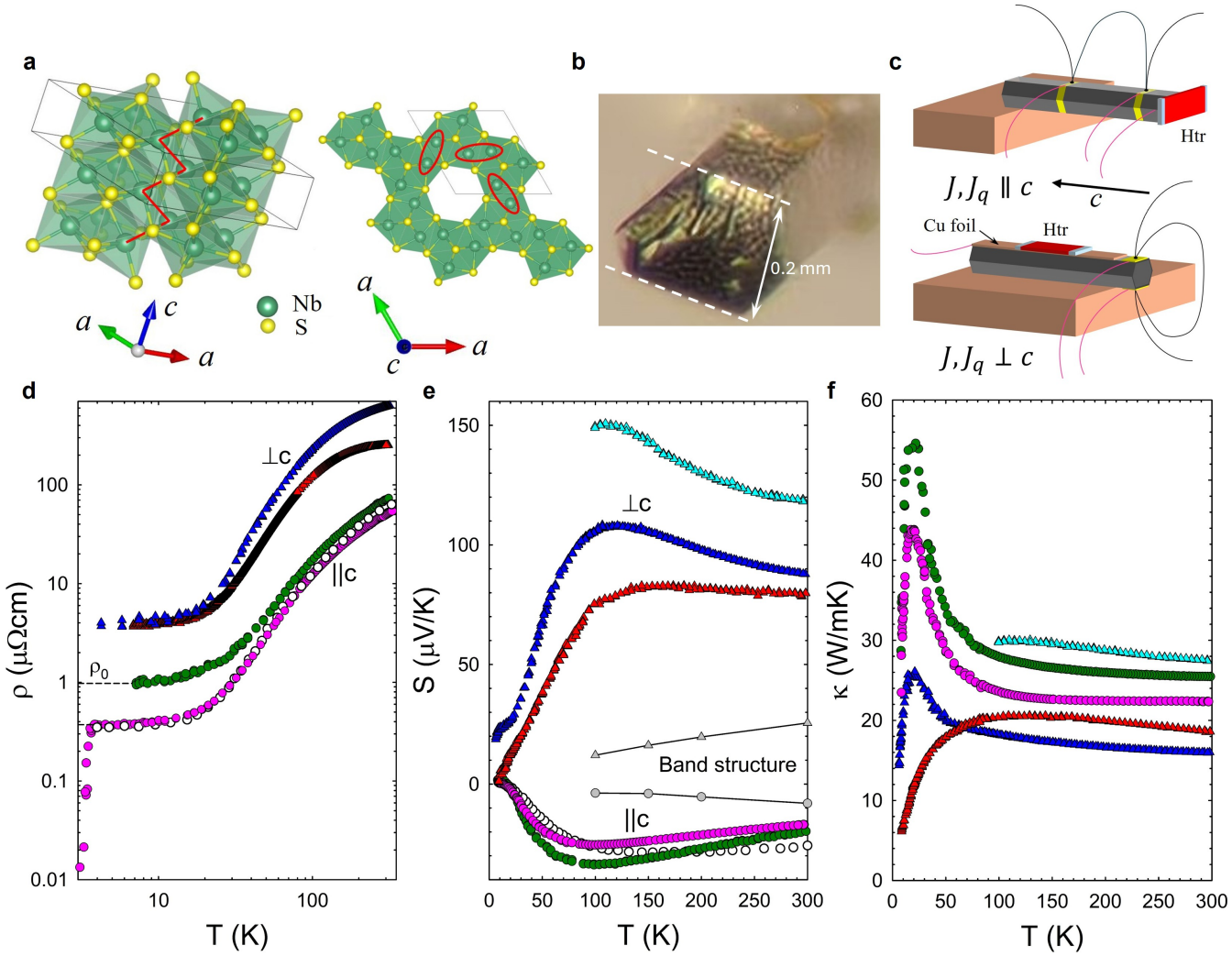


Fig. 1 | Transport properties and axis-dependent thermopower polarity. a, Hexagonal structure of Nb_3S_4 highlighting one of three zigzag Nb-Nb chains per unit cell along the c axis (left) and packing of the face-sharing NbS_6 distorted octahedra in the hexagonal planes (right). Ovals on the right encircle Nb atoms of the zigzag chains. The black lines mark the unit cell (rendered with VESTA software, Ref. 13). **b**, Photo of a Nb_3S_4 crystal showing typical transverse dimensions. **c**, Schematic of measurement configuration for the two current orientations. **d-f**, Resistivity, thermopower, and thermal conductivity for Nb_3S_4 crystals (solid circles, $||c$; triangles, $\perp c$), open circles are from Refs. 14, 15. The calculated thermopower is represented by symbols and lines.

$|\alpha|$ values for Nb_3S_4 along both directions rival or exceed those of the other compounds in this low-T regime. The same is true for the axial power factors, $PF = S^2/\rho$, which exceed $100\mu W/cmK^2$ at 50 K (Supplementary Fig. S4).

To compute the transverse thermoelectric parameters, we consider x-y coordinates rotated by angle ϕ with respect to the a-c axes. A temperature gradient $\nabla_x T$ along the x-direction produces an electric field along y, $E_y = S_{yx}\nabla_x T$ with $S_{yx} = (S_a - S_c)\sin\phi\cos\phi$. The transverse Peltier conductivity is defined as $\alpha_{yx} = \sigma_{yx}S_{xx} + \sigma_{yy}S_{yx}$, and figure of merit, $z_{yx}T = S_{yx}^2 T/\left(\rho_{yy}\kappa_{xx}\right)$. α_{yx} has its maximum value at $\phi = 45°$ and is plotted using data for the three different $J_q \perp c$ crystals in Fig. 2b. The optimum ϕ maximizing $z_{yx}T$ is computed from[4] $\cos^2\phi_{opt} = \left[1 + \sqrt{(\kappa_c/\kappa_a)/(\rho_c/\rho_a)}\right]^{-1}$ and is only weakly dependent on temperature (Fig. 2d), with ϕ values at 150 K employed to compute the $z_{yx}T$ curves in Fig. 2c (tensor expressions within the x-y coordinate system are presented in Supplementary Section S4).

Nernst effects, both ordinary and anomalous, represent alternative mechanisms for transverse thermoelectric technology. The ordinary Nernst effect in $Bi_{1-x}Sb_x$ compounds, yielding $z_{yx}T \sim 0.35$ at 200 K (dashed curve, Fig. 2c) in a magnetic field [19] $\lesssim 1$ T, has served for decades as a benchmark for technological significance. The anomalous Nernst effect has received considerable attention in the last several years [20] with substantial transverse Peltier conductivities and figures of merit reported, originating from both intrinsic (topological Berry curvature) and extrinsic (magnon interactions with charge carriers) mechanisms. A clear disadvantage of the Nernst effect generally is the requirement of an applied magnetic field. For comparison, we

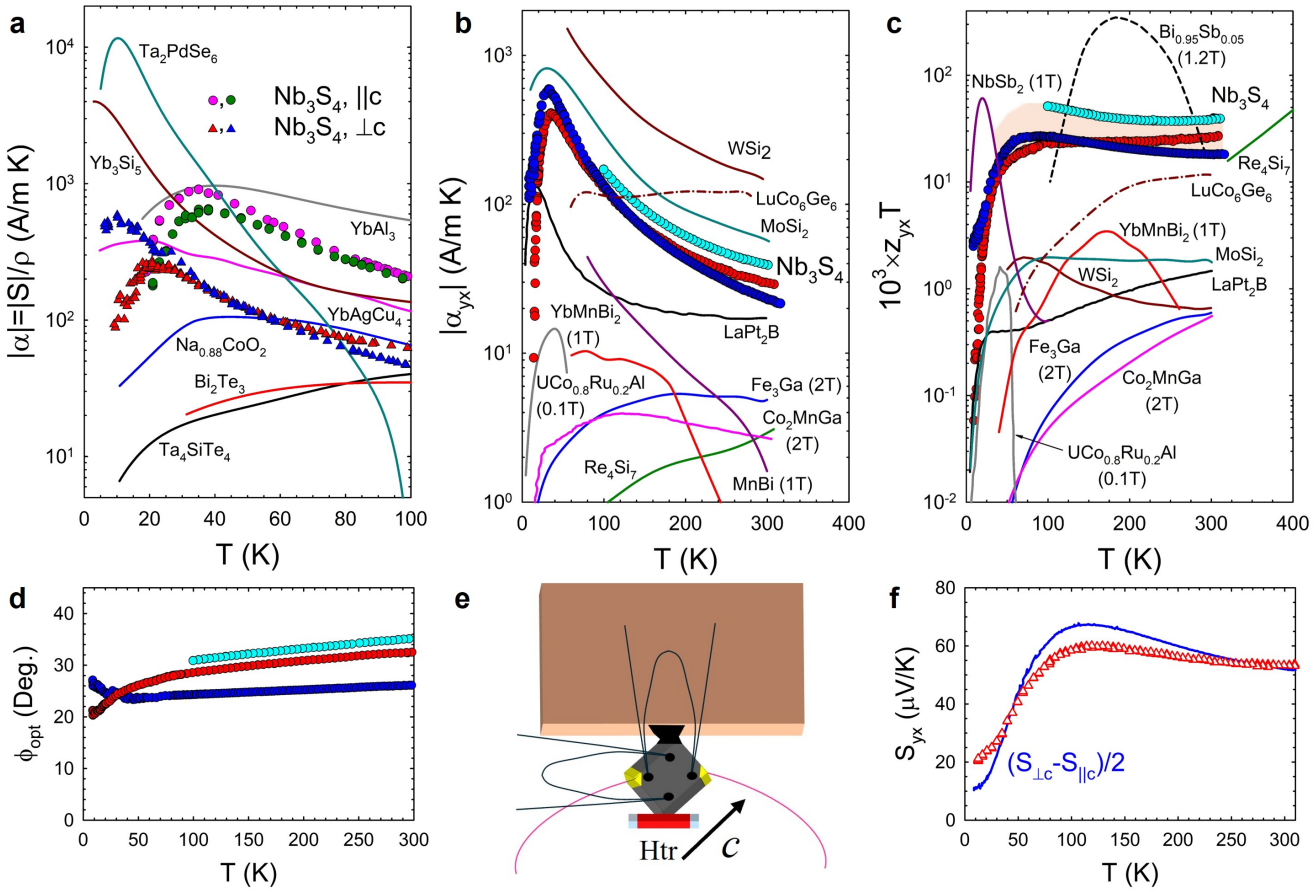


Fig. 2| Exceptional axial and transverse Peltier conductivities, and thermoelectric performance. Axial (**a**) and transverse (**b**) Peltier conductivities, and transverse figure of merit (**c**) for the Nb_3S_4 crystals from Fig. 1 compared to those (curves) of a variety of other materials (see Supplementary information Tables S2, S3 for references). Curves in **b** and **c** for which a magnetic field value is listed in parentheses correspond to Nernst effect data. The three different symbols in **b** and **c** were computed using the three $S_{\perp c}$ data sets from Fig. 1b, and the shaded region in **c** reflects the spread in their values propagated to $z_{yx}T$. **d**, Optimum ϕ angles for maximizing $z_{yx}T$ computed using the axial S measurements. **e**, Setup for the direct S_{yx} measurement. **f**, Measured $S_{yx}(T)$ (triangles) compared to $(S_{\perp c} - S_{\|c})/2$ (solid curve).

include data for a number of these materials for which the applied field is $\lesssim 2$ T in Figs. 2b and c. Also included are recently discovered ADCP metals having large transverse Peltier conductivities ($LaPt_2B$, WSi_2, $MoSi_2$, $LuCo_6Ge_6$), but substantially lower $z_{yx}T$ than Nb_3S_4.

To confirm the transverse thermoelectric effect, we measured $S_{yx}(T)$ directly (Methods and Supplementary Fig. S5) for a piece with similar b and c dimensions, cut from the crystal represented by blue triangles in Fig. 1, oriented with heat current and transverse voltage contacts aligned at $\sim 45°$ with respect to the crystal axes (Fig. 2e). Good agreement is found with the $S_{yx}(T)$ computed from the axial Seebeck coefficients and tensor expressions in the rotated coordinate system (solid curve, Fig. 2f).

To understand the origin of the exceptional ADCP behavior of Nb_3S_4 we computed the electronic structure from density functional theory and transport coefficients based on the linearized Boltzmann equations (Methods) under the constant relaxation time approximation (CRTA). Figure 3a shows the energy bands along high symmetry directions and density of states (right panel); the Brillouin zone is depicted in Fig. 3b. Four bands cross E_F, representing a mixed dimensionality in combination (designated $\alpha - \delta$); overall the bands are in good agreement with results from prior computational studies [21–23]. A photoemission intensity projection of the Fermi surface (FS) within the $\Gamma - A - M - L$ plane from the only known such study [24] agrees reasonably well with the computed FS (Supplementary Fig. S6).

FS color maps in Fig. 3c-f and g-j represent inverse effective masses normalized to the free-electron value and components of the Fermi velocity, respectively, along the out-of-plane ($\|c$) and in-plane ($\perp c$) directions. Negative values for $1/m^*$ correspond to holes and $1/m^*_{\perp c} \equiv (1/m^*_a + 1/m^*_b)/2$. FS sheets β and γ (isolated in Figs. 3d, f, h, j) are predominant in conduction $\|c$ and $\perp c$, respectively, as is evident in the near coincidence of their respective smallest-mass and highest-velocity regions in the FS maps. Overall, the FS sheets have mixed electron-hole character with hole-like

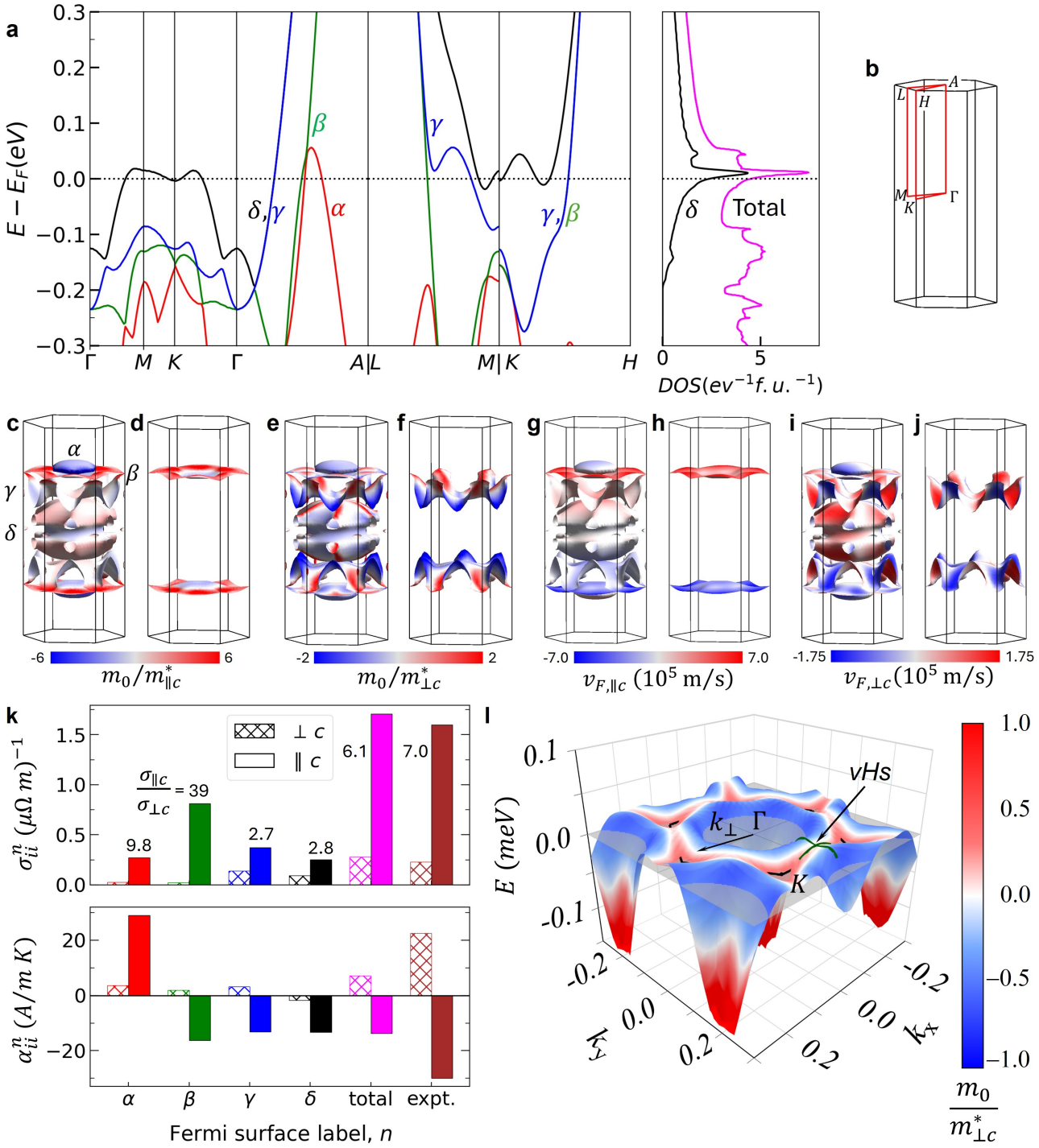


Fig. 3| Density-functional theory predicts ADCP and extended van Hove singularity near E_F a, DFT band dispersions along high-symmetry directions and density of states (the Brillouin zone is shown in **b**), Fermi surface maps showing components of the inverse effective mass tensor (**c-f**) and velocity (**g-j**) both $\|c$ and $\perp c$, **k**, Calculated axial, band-specific electrical (σ^n_{ii}, upper panel) and Peltier (α^n_{ii}, lower panel) conductivities at 300 K along each direction compared to experiment (using averaged values for each direction from Fig.1), and **l**, 3D contour plot of the in-plane dispersions for band δ at $k_z = 0$ with color map of the inverse effective masses. $k_\perp$ is the in-plane momentum position of an extended region of nearly-localized states associated with the van Hove singularity saddle point (label vHs, arrow and curves) underlying the sharp density of states peak near E_F.

portions primarily composed of in-plane bonds between Nb d_{xy}, $d_{x^2-y^2}$, d_{xz}, and d_{yz} orbitals and S p_x and p_y orbitals, while electron-like regions are dominated by Nb d_{z^2}, d_{xz}, and d_{yz} orbitals bonding along the Nb chains (Supplementary Fig. S7). The computed band electrical conductivities at 300 K, assuming a constant relaxation time $\tau_0 = 10^{-14}$ s, are shown in Fig. 3k (upper panel) along with the ratio for each band, $\sigma_{\|c}/\sigma_{\perp c}$. The most one-dimensional FS sheet β corresponds to the most linear and dispersive band along c^*, crossing approximately midway along the paths $\Gamma - A$, $M - L$, and $K - H$ in Fig. 3a. Its computed conductivity ratio at 300 K, is $\sigma_{\|c}/\sigma_{\perp c} \simeq 39$. The ovate hole pocket (α) is also highly anisotropic, with $\sigma_{\|c}/\sigma_{\perp c} \simeq 10$. The other bands have substantially smaller anisotropy and larger phase-space weight such that the total computed conductivity anisotropy is $\sigma_{\|c}/\sigma_{\perp c} \simeq 6.1$, comparing favorably to the ratio (7.0) of the averaged experimental results for each direction.

The computed band-specific axial Peltier conductivities at 300 K (Fig. 3k, lower panel), reveal that β and γ are goniopolar, while band α (δ) is hole-like (electron-like) in both directions. The sum of the band Peltier conductivities yields the total axial Peltier conductivity for each direction. Significantly, these values, 7.5 A/mK (-13 A/mK) for the $\perp c$ ($\|c$) directions, are a factor of 2-3 smaller than the measured values 22.5 A/mK (-30 A/mK) (far right bars of Fig. 3k). Similar or larger discrepancies are found between the computed and measured axial thermopowers (Fig. 1e). The computed maximum transverse Peltier conductivity (for $\phi = 45°$) is $\alpha_{yx} = (\alpha_{\perp c} - \alpha_{\|c})/2 = 10.3$ A/mK, also a factor of 2-4 larger than found in experiment (Fig. 2b). The computed ADCP behavior was found to persist, for $T \geq 150$ K, with shifts of E_F in the range -20 meV to +50 meV relative to the DFT value (assuming rigid bands). A maximum in the computed $S_{\perp c} - S_{\|c} \simeq 36\mu$V/K occurs,for 300 K, near a +25 meV shift but remains substantially smaller than observed in experiment (Supplementary Fig. S8).

The CRTA is typically a good approximation at room temperature, even for complex metals, because phonon-induced scattering events involve large momentum transfers, and the transition probability integrates over virtually all final states on the Fermi surface. A notable exception is the case of interband transitions between dispersive and more-localized overlapping bands where, via Fermi's Golden Rule, the scattering rate is proportional to the density of final states. This characteristic, in combination with matrix elements sensitive to the orbital and dominant phonon symmetries, can result in band-dependent and anisotropic scattering rates.

The exceptional thermoelectric properties of Nb_3S_4 appear to arise from precisely this scenario, evidenced by the sharp, narrow density of states peak just 10.2 meV above E_F (right panel, Fig. 3a), a robust feature of the electronic structure entirely attributable to an extended region of nearly-localized states associated with a van Hove singularity (vHS) within band δ near the M point. Figure 3l shows a three-dimensional plot of the in-plane dispersions for this band at $k_z = 0$ (within the $\Gamma - M - K$ plane), with color shading representing the inverse effective masses. The nearly-localized states (where $\nabla_k E, m_0/m^* \rightarrow 0$) occupy the momentum range between a circle of radius $k_\perp$ and the BZ boundary (Fig. 3l), extending along c^* to $k_z \simeq 0.05(\pi/c)$ and representing $\sim 2.2\%$ of the BZ volume (Supplementary section S8 and Figs. S9, S10). The peak in the density of states is well approximated by a Lorentzian centered at 10.2 meV with half-width 6.3 meV (Supplementary section S9, Fig. S11).

These nearly localized states can play a major role in transport through their effect on electron scattering – given their proximity to E_F, significant interband scattering into these states can occur for carriers in dispersive states that interact with phonons of appropriate wavenumber and symmetry over an extended energy range (10.2 ± 6.3 meV). The resulting energy-dependent scattering time (τ), asymmetric about E_F, can substantially enhance and even change the sign of the Seebeck coefficient reflected in DFT calculations, as illustrated by the Mott form [25] for the Seebeck tensor,

$$S_{ij} = -\frac{\pi^2 k_B^2 T}{3|e|} \left\{ \frac{L'_{ij}(\epsilon)}{L_{ij}(\epsilon)}\bigg|_{E_F} + \frac{\tau'_{ij}(E)}{\tau_{ij}(E)}\bigg|_{E_F} \right\},$$

where L_{ij} is the transport distribution function (Methods) and "$\prime$" represents the energy derivative. A simple model wherein τ_{ij} is inversely proportional to the density of nearly-localized states for the δ band yields a scattering term $\tau'/\tau < 0$ comparable to or greater in magnitude than the band structure term in L_{ij} for all bands and directions (Supplementary Section S9, Fig. S11 and Table S5). Anisotropy in the electron-phonon coupling dictating band-specific scattering times is anticipated, and stronger scattering for states with momenta $\perp c$ would be needed to simultaneously enhance the computed thermopowers to match experiment while maintaining ADCP character. Notably, the intrinsic T-dependent resistivity for both transport directions behaves as $\rho(T) - \rho_0 \propto T^n$, $n \simeq 3$ at $T \lesssim 60$ K (Supplementary section S10, Fig. S12). This Bloch-Wilson form [26, 27] is expected for interband scattering from dispersive to nearly-localized states, and the observed T range is consistent with the calculated phonon spectrum (Supplementary section S11, Fig. S13). For transport $\|c$, electron-electron Umklapp scattering can also yield a similar power-law behavior [14, 28] (Supplementary section S10); both mechanisms may be relevant in Nb_3S_4. These observations can be further refined with calculations of the electron-phonon coupling.

Practical application of Nb_3S_4, and other potential ADCP materials with similar characteristics, will benefit from larger crystals or possibly epitaxially-grown thin films. It is notable that the closely related compounds having Se or Te in place of S may also possess exceptional ADCP character, as suggested by preliminary calculations [29], but the available crystals thus far are needle-like and thus transport $\perp c$ has not been accessible to experiment. An additional lever for potential applications is the open crystal structure of these compounds which permits intercalation [30] (e.g., with other metals) that can be employed to tune E_F. The combination of mixed-dimensional electronic structure and strong energy-dependent scattering associated with an extended vHs near E_F are key ingredients underlying the exceptional transverse thermoelectric properties reported

here and define new design parameters for the discovery of other materials.

[1] Goldsmid, H. Application of the transverse thermoelectric effects. *J. Electron. Mater.* **40**, 1254 (2011).

[2] Adachi, H., Ando, F., Hirai, T., Modak, R., Grayson, M. A. & Uchida, K-I. Fundamentals and advances in transverse thermoelectrics. *Appl. Phys. Express* **18**, 090101 (2025).

[3] Feng, T., Zhou, Z., Wang, P., Liao, Z., Wang, Y., Zhao, H., Zhang, W. & Liu, W. Transverse thermoelectric materials: Recent advances and challenges. *Next Energy* **3**, 100105 (2024).

[4] Zhou, C., Birner, S., Tang, Y., Heinselman, K. & Grayson, M. Driving perpendicular heat flow: $(p \times n)$-type transverse thermoelectrics for microscale and cryogenic Peltier cooling. *Phys. Rev. Lett.* **110**, 227701 (2013).

[5] He, B., Wang, Y., Arguilla, M. Q., Cultrara, N. D., Scudder, M. R., Goldberger, J. E., Windl, W. & Heremans, J. P. The Fermi surface geometrical origin of axis-dependent conduction polarity in layered materials. *Nat. Mater.* **18**, 568 (2019).

[6] Song, T. & Goldberger, J. E. A Field Guide to Materials with Axis-Dependent Conduction Polarity, *Chem. Mater.* **37**, 7518-7533 (2025).

[7] Yang, Z., He, X., Usui, H., Kamiya, T. & Katase, T. Axis-Dependent Conduction Polarity: Design Principles and High-Throughput Discovery of Transverse Thermoelectrics. *J. Am. Chem. Soc.* **148**, 6704-6715 (2026).

[8] Cohn, J. L., Moshfeghyeganeh, dos Santos, S., C. A. M. & Neumeier, J. J. Extreme Thermopower Anisotropy and Interchain Transport in the Quasi-One-Dimensional Metal $Li_{0.9}Mo_6O_{17}$. *Phys. Rev. Lett.* **112**, 186602 (2014).

[9] Graziosi, P., Mehnert, K.-I., Dutt, R., Bos, J.-W. G. & Neophytou, N. Materials design criteria for ultrahigh thermoelectric power factors in metals. *PRX Energy* **3**, 043009 (2024).

[10] Garmroudi, F. *et al.* Energy filtering–induced ultrahigh thermoelectric power factors in Ni_3Ge. *Sci. Adv.* **11**, eadv7113 (2025).

[11] Ruysink, A. F. J., Kadijk, F., Wagner, A. J., & Jellinek, F. Preparation, structure and properties of triniobium tetrasulphide, Nb—$3S_4$. *Acta Crystallogr., Sect. B: Struct. Crystallogr. Cryst. Chem. B* **24**, 1614 (1968).

[12] Nakada, I. & Ishihara, Y. Preparation of a quasi-one-dimensional Nb_3S_4 crystal. *Jap. J. Appl. Phys.* 2**3**, 677-680 (1984).

[13] Momma K. & Izumi, F. VESTA 3 for three-dimensional visualization of crystal, volumetric and morphology data. *J. Appl. Crystallogr.* **44**, 1272 (2011).

[14] Ishihara, Y. & Nakada, I. Electrical conduction of a quasi-one dimensional Nb_3S_4 single crystal. *Sol. St. Commun.* **42**, 579 (1982).

[15] Ishihara, Y., Nakada, I., Suzuki, K. & Ichihara, M. Thermoelectric power of quasi-one-dimensional Nb_3X_4, with X= S, Se, and Te. *Sol. St. Commun.* **50**, 657 (1984).

[16] Amberger, E., Polbom, K., Grimm, P., Dietrich, M. & Obst, B. Superconductwity in the Nb cluster compounds $Nb_3(x, y)_4$ with $X,\ Y =$ S, Se, Te. *Sol. St. Commun.* **26**, 943 (1978).

[17] Biberacher, W. & Schwenk, H. Critical field and specific heat of the anisotropic superconductor Nb_3S_4. *Sol. St. Commun.* **33**, 385-387 (1980).

[18] Okamoto, H. & Ishihara, Y. Specific heat of an anisotropic superconductor: Nb_3S_4. *Phys. Rev.* B **48**, 3927-3932 (1993).

[19] Jandl, P., Birkholz, U. Thermogalvanomagnetic properties of Sn-doped $Bi_{95}Sb_5$ and its application for solid state cooling. *J. Appl. Phys.* **76**, 7351-7366 (1994).

[20] Pan, Y., He, Bin, Wang, H., & Felser, C., Topological materials for high performance transverse thermoelectrics. *Next Energy* **2**, 100103 (2024), and references therein.

[21] Oshiyama, A. Energy bands and fermi surfaces of quasi-one-dimensional transition metal chalcogenides Nb_3X_4. *Sol. St. Commun.* **43**, 607-612 (1982).

[22] Canadell, E. & Whangbo, M.-H. Electronic Structure of Nb_3X_4 Type Compounds. *Inorg. Chem.* **25**, 1489 (1986).

[23] Materials Data on Nb_3S_4 (mp-12627) by Materials Project. United States. doi:https://doi.org/10.17188/1189092

[24] Dobashi, T. , Sato, T., Souma, S., Takahashi, T., Kaneko, H., Ishihara, Y. & Okamoto, H. Electronic structure of quasi-one-dimensional conductors Nb_3X_4 (X=S,Se,Te) studied by angle-resolved photoemission spectroscopy. *Phys. Rev. B* **76**, 045121 (2007).

[25] Cutler, M. & Mott, N. F. Observation of Anderson localization in an electron gas. *Phys. Rev.* **181**, 1336–1340 (1969).

[26] Wilson, A. H. The electrical conductivity of the transition metals, *Proc. R. Soc. Lond. A. Math. Phys. Sci.* **167**, 580–593 (1938).

[27] Garmroudi, F., Yan, X., Paschen, S., Thomas, S. M., Bauer, E. D., Pustogow, A. & Rosa, P. F. S. Tracking flat bands via phonon-mediated interband scattering. arXiv:2508.16491 (2025).

[28] Oshiyama, A. Electronic structure of quasi-one-dimensional transition metal chalcogenide Nb_3X_4. *J. Phys. Soc. Jpn.* **52**, 587-596 (1983).

[29] Rahman, S., Akopyan, A., Bhagade, S., Neumeier, J. J. & Cohn, J. L. unpublished.

[30] Scholz, G. A. Inducing a CDW ground state in Nb_3Se_4 by intercalation. *Sol. St. Ionics* **149**, 131-138 (2002).

[31] Giannozzi, P. *et al.* QUANTUM ESPRESSO: a modular and open-source software project for quantum simulations of materials. *J. Phys.: Condens. Matter* **21**, 395502 (2009).

[32] Madsen, G. K. H., Carrete, J. & Verstraete, M. J. BoltzTraP2, a program for interpolating band structures and calculating semiclassical transport coefficients. *Comp. Phys. Commun.* **231**, 140–145 (2018).

[33] Kawamura, M. FermiSurfer: Fermi-surface viewer providing multiple representation schemes. *Comp. Phys. Commun.*, **239**, 197-203 (2019).

Experimental Section/Methods

Crystal growth

Single crystals of Nb_3S_4 were grown using iodine transport. Approximately 2 g of elemental niobium and sulfur mixed in stoichiometric ratio were combined with $\sim$ 100 mg of iodine. The mixture was placed on one side of a sealed, evacuated quartz ampoule with 12 mm inner diameter and 18 cm length. The side containing the mixture was placed in the center of a single-zone tube furnace to establish a temperature gradient. The temperature was ramped up to 1050°C over 24 hours and held there for 25 days before cooling over an additional 2 days. The resultant crystals were washed in deionized water and dried in acetone.

Crystal structure and stoichiometry

A Philips X'Pert x-ray diffractometer (Cu K_α, $\lambda = 1.54056$ Å) was employed in determining the crystallographic structure. Lattice parameters for the hexagonal unit cell were determined from high-angle extrapolation of reflections from the (h00) and (h0h) lattice planes (Fig. S2). Electron dispersive spectroscopy (EDS) was employed for several crystals to assess stoichiometry and uniformity of composition, with each crystal scanned over a minimum of 3 locations and the corresponding compositions averaged. No significant variation in composition was detected among the different crystals studied (Table S1).

Transport property measurements

Individual crystals with typical dimensions $4\times0.3\times0.2$ mm^3 were prepared with four sputtered gold electrical contacts (two for the measurement $\perp c$) deposited through shadow masks on each of the opposing crystal faces (Fig. 1 c). For c-axis measurements, shorting of the contacts on opposing faces ensured axial electric current flow. A steady-state (two-thermometer, one-heater) method was employed in a radiation-shielded vacuum probe to measure the thermopower and thermal conductivity. Specimens were suspended from a Cu heat sink and affixed with a fine-wire chromel-constantan thermocouple and a 1 kΩ chip heater on the free end. The accuracy of the measured κ is $\sim$ 10 %, dictated by uncertainty in the measured separation between thermocouple junctions. Corrections have been applied for losses due to radiation and conduction through the leads which were measured separately on a variety of materials with similar geometric factors and thermal conductances. These losses were 10-15% at 300 K and $\lesssim$ 2 % at $T < 100$ K.

For the direct measurement of S_{yx} (Fig. 2e, f), steady-state measurement of the transverse voltage (ΔV_y) and both the longitudinal (ΔT_x) and transverse (ΔT_y) thermocouple voltages (Supplementary Fig. S5), allowed S_{yx} to be computed as,

$$S_{yx} = \frac{\Delta V_y}{\Delta T_x}\frac{\ell_{TC}}{w_V} - \left(S_{yy} - S_{Au}\right)\frac{\Delta T_y}{\Delta T_x}\frac{\ell_{TC}}{w_{TC}},$$

where ℓ_{TC}, w_{TC} and w_V are the separations of the longitudinal and transverse thermocouple junctions, and transverse voltage contacts, respectively, and $S_{yy} = (S_{\perp c} + S_{\parallel c})/2$ (for $\phi = 45°$) and S_{Au} is the small thermopower of the lead wires.

Ab initio calculations

Electronic structure calculations were performed using density functional theory (DFT) as implemented in the Quantum ESPRESSO package [31], employing scalar-relativistic Optimized Norm-Conserving Vanderbilt pseudopotentials with the Perdew-Burke-Ernzerhof exchange-correlation functional within the Generalized Gradient Approximation. Experimental lattice parameters obtained from x-ray diffraction measurements were used throughout. Kinetic energy cutoffs of 150 Ry and 900 Ry were adopted for the plane-wave basis set and charge density, respectively. A Monkhorst-Pack k-point mesh of $16\times16\times38$ was employed for the self-consistent field calculations, chosen to ensure uniform sampling density across all reciprocal space directions; the energy cutoffs and k-mesh were validated through structural relaxation and systematic convergence tests by monitoring the total energy. A subsequent non-self-consistent field (NSCF) calculation was carried out on a denser $24\times24\times58$ k-mesh to obtain the electronic band structure over a finer grid suitable for transport analysis. Transport coefficients were computed within the semiclassical Boltzmann transport equation framework under the relaxation time approximation using the BoltzTraP2 code [32], which interpolated the NSCF eigenvalues onto a mesh approximately 20 times denser to ensure convergence of the transport integrals. Fermi surface maps were rendered using FermiSurfer [33].

Using the energy of the nth band at point $\mathbf{k}$, $\epsilon_{\mathbf{k},n}$, the transport distribution function was computed as,

$$L_{ij}(\epsilon) = \sum_n L^n_{ij}(\epsilon) = \sum_n \sum_k v_i v_j \tau_0 \delta(\epsilon - \epsilon_{n,\mathbf{k}})$$

where L^n_{ij} is the partial transport distribution function tensor of the nth band, v_i is the ith component of the band velocity, $\mathbf{v} = (1/\hbar)\nabla_{\mathbf{k}}\epsilon_{n,\mathbf{k}}$, $\tau_0 (= 10^{-14}$ s) is the relaxation time, and δ is the delta function.

The partial electrical and Peltier conductivity tensors were then computed as,

$$\sigma^n_{ij} = e^2 \int_{-\infty}^{\infty} d\epsilon \left(-\frac{\partial f}{\partial \epsilon}\right) L^n_{ij}(\epsilon)$$
$$\alpha^n_{ij} = (\sigma^n S^n)_{ij} = \frac{-e}{T}\int_{-\infty}^{\infty} d\epsilon \left(-\frac{\partial f}{\partial \epsilon}\right)(\epsilon - \mu) L^n_{ij}(\epsilon),$$

where e is the magnitude of the electron charge, S^n_{ij} is the Seebeck tensor for the nth band. The total electrical and Peltier conductivities are obtained as sums of their band-specific tensors. The axial thermopower for the ith direction is obtained as, $S_{ii} = (\sigma S)_{ii}/\sigma_{ii}$.

The inverse mass tensor of the nth band was computed as,

$$\left[\frac{1}{m^*}\right]_{ij} = \frac{1}{\hbar^2}\frac{\partial^2 \epsilon_{n\mathbf{k}}}{\partial k_i \partial k_j}.$$

Data availability

Data supporting the findings of this study are included in this article and its Supporting Information or available from the corresponding authors on request.

Acknowledgements

This material is based on work supported by the U.S. Department of Energy, Office of Basic Energy Sciences, Division of Materials Science and Engineering under grant No. DE-SC0008607 (Univ. Miami) and the National Science Foundation under Award DMR-2411583 (Montana St. Univ.). The authors acknowledge S. M. Alawfi and D. Takshi for assisting with transport measurements and DFT calculations, respectively.

Author contributions

S. B. characterized single-crystal specimens and conducted transport measurements. M. S. R. performed the ab initio and transport property calculations. A. A. assisted with and supervised specimen characterization, preparation, transport measurements and ab initio and transport property calculations. P. W. grew the single crystals and carried out their initial characterization and J. J. N. supervised that work. J. J. N. and J. L. C. conceived of the project. J. L. C. supervised the work at Univ. Miami and drafted the manuscript with input from S. B., M. S. R, and A. A. All authors discussed the results and reviewed the manuscript.

Competing interests

The authors declare no competing interests.

Supporting information

Supporting Information is available from the Wiley Online Library or from the author.

Supporting Information for:

"Axis-dependent polarity and extended van Hove singularity for exceptional transverse thermoelectricity"

S. Bhagade, M. Shahnoor Rahman, A. Akopyan, P. White, J. J. Neumeier, and J. L. Cohn

S1. Transport data for additional crystals

Transport data $\|c$ for three additional crystals are shown in Fig. S1. Consistent with the data presented in Fig. 1, there is considerable variation in the thermal conductivities among crystals that have very similar resistivities and thermopowers. As noted in the main text and identified in x-ray scattering in the next section, variations in the lattice thermal conductivities are the likely explanation, associated with structural defects (e.g., low-angle misorientations of the hexagonal planes of several crystallites).

In the absence of Hall measurements from the literature, a rough estimate of the anticipated carrier density can be made by assuming a formal oxidation state of S^{2-} which dictates a fractional, average oxidation state of +2.67 for each Nb. The remaining 2.33 electrons per Nb are available for conduction, given the partially filled and overlapping Nb 4*d* orbitals, resulting in a maximum of 7 electrons per formula unit or 14 per unit cell (2 f.u. per cell). With a unit cell volume $V \simeq 268.4$ Å^3, the maximum carrier density is then estimated as $n \simeq 5.2 \times 10^{22}/\text{cm}^3$.

S2. X-ray scattering and crystal composition

A Philips X'Pert x-ray diffractometer (Cu K_α, $\lambda = 1.54056$ Å) was employed in determining the crystallographic structure. Lattice parameters for the hexagonal unit cell were determined from high-angle extrapolation [1] of reflections from the $(h00)$ and $(h0h)$ lattice planes as shown in Fig. S2 a for five crystals. Both lattice constants were the same within uncertainties for all crystals studied, $a = 9.581(1)$ Å, $c = 3.376(1)$ Å.

Some crystals exhibited evidence of multiple crystallites, aligned along their c axes, but with low-angle rotations of their hexagonal planes about c. Rocking curve (ω) and ϕ scans of the (020) reflection for one such crystal are shown in Fig. S2 b, c (the inset in c depicts the misaligned hexagons, with angles exaggerated). The transport data for this crystal are included in Fig. 1 as red triangles. The x-rayed surface of this crystal was less shiny, distinguishing it from its other faces and from those of others crystals investigated. Other crystals exhibited similar features in ω and ϕ scans of $(h, nh, 0)$ planes with $n = 2, 3, 4$, but typically with a smaller spread in angle than those of Fig. S2 b, c, suggesting a narrower distribution of rotation angles. The other crystals for which transport is presented in Fig. 1 exhibited no such features in x-ray scans or on surfaces under optical inspection, but given that the x-ray scattering penetration depth is limited to $\sim 50\mu$m, this does not preclude the presence of similar defects in a portion of the volume for other crystals.

Electron dispersive spectroscopy (EDS) studies of three crystals yielded compositions shown in Table S1. Each composition reflects the average of scans from at least three locations. The values suggest a composition for the crystals that is modestly Nb poor and S rich compared to the stoichiometric values, Nb=42.9 At%, S=57.1 At%, suggesting the presence of Nb

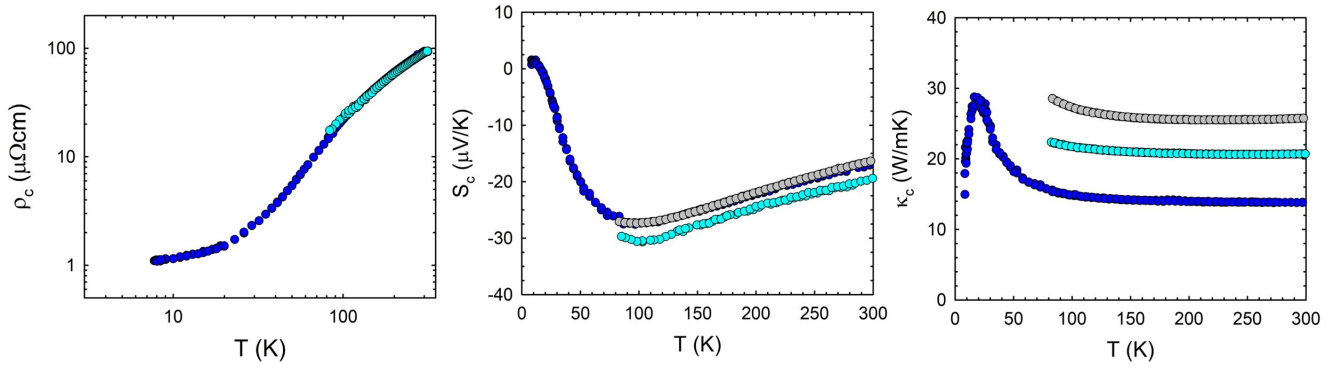


Fig. S1| Transport properties for additional crystals. Resistivity, thermopower and thermal conductivity data along the c-axis for additional crystals.

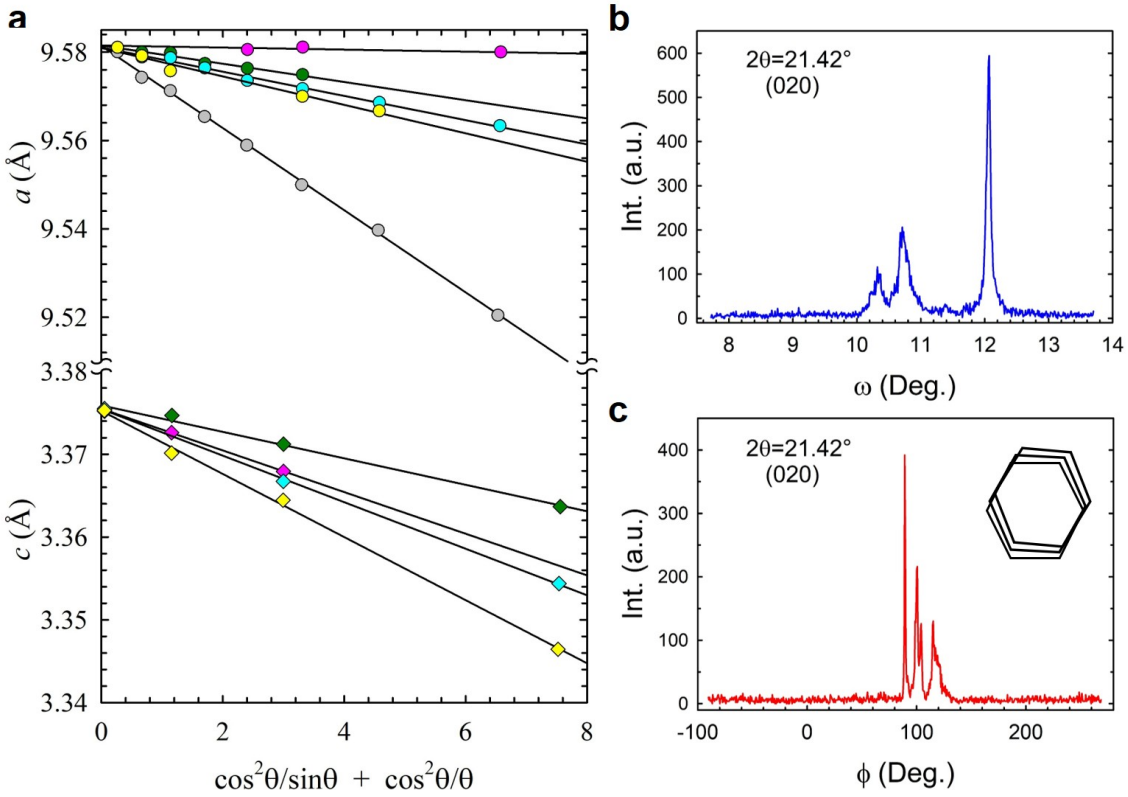


Fig. S2| Lattice constant determinations and crystal defects. a, High-angle extrapolation of reflections of different order from the (h00) (upper panel) and (h0h) (lower panel) planes for 5 crystals used to determine precision lattice constants a and c. Solid lines are linear-least squares fits. Rocking curve (**b**) and ϕ scan (**c**) of the (020) reflection for the crystal designated by red triangles in Fig. 1. The inset in **c** depicts slightly misaligned hexagonal planes of multiple crystallites implicated in the scans.

TABLE S1| EDS compositions and lattice constants for three crystals for which both were measured. Color of the symbols for transport data from Fig. 1 are listed in parentheses for two crystals. Uncertainties in the compositions reflect standard deviations in measurements from a minimum of three EDS locations on the crystal surface.

Crystal	Nb (At%)	S (At%)	Nb/S	a (Å)	c (Å)
Crystal 1 (pink)	41.6(5)	58.4(5)	0.71(1)	9.581(2)	3.375(1)
Crystal 2 (green)	40.3(12)	59.7(12)	0.68(3)	9.581(3)	3.376(1)
Crystal 3	40.5(6)	59.5(6)	0.68(2)	9.581(3)	3.375(1)

vacancies. However, the apparent deviation from stoichiometry ($\lesssim 10\%$) is more likely a systematic error associated with deconvolution of the overlapping Nb L_α and S K_α x-ray lines employed in semiquantitative, standardless EDS.

S3. Estimate of electronic and lattice contributions to the thermal conductivity

To approximately separate the electronic (κ_e) and lattice (κ_L) contributions to κ for the two c-axis crystals shown in Fig. 1, the electronic component was calculated using the model of Makinson [2] which accounts for the deviation of the electronic Lorenz number (L_e) in simple metals from the Sommerfeld value, $L_0 = (\pi^2/3)(k_B/e)^2$, at intermediate temperatures due to scattering of electrons from equilibrium longitudinal phonons,

$$L_e \equiv \frac{\kappa_e}{\sigma T} = \frac{\rho_0/4A + (T/\Theta)^5 \mathscr{J}_5}{\rho_0/4A + \chi(T/\Theta, N_a)},$$

where A is an empirical impurity parameter, obtained for each crystal by a linear fit (Fig. S3 a) of its intrinsic resistivity [2], $\rho_i(T) = \rho - \rho_0 \equiv A(T/\Theta)$, $\Theta = 360$ K is the Debye temperature [3], and χ and $\mathscr{J}_5$ are defined as,

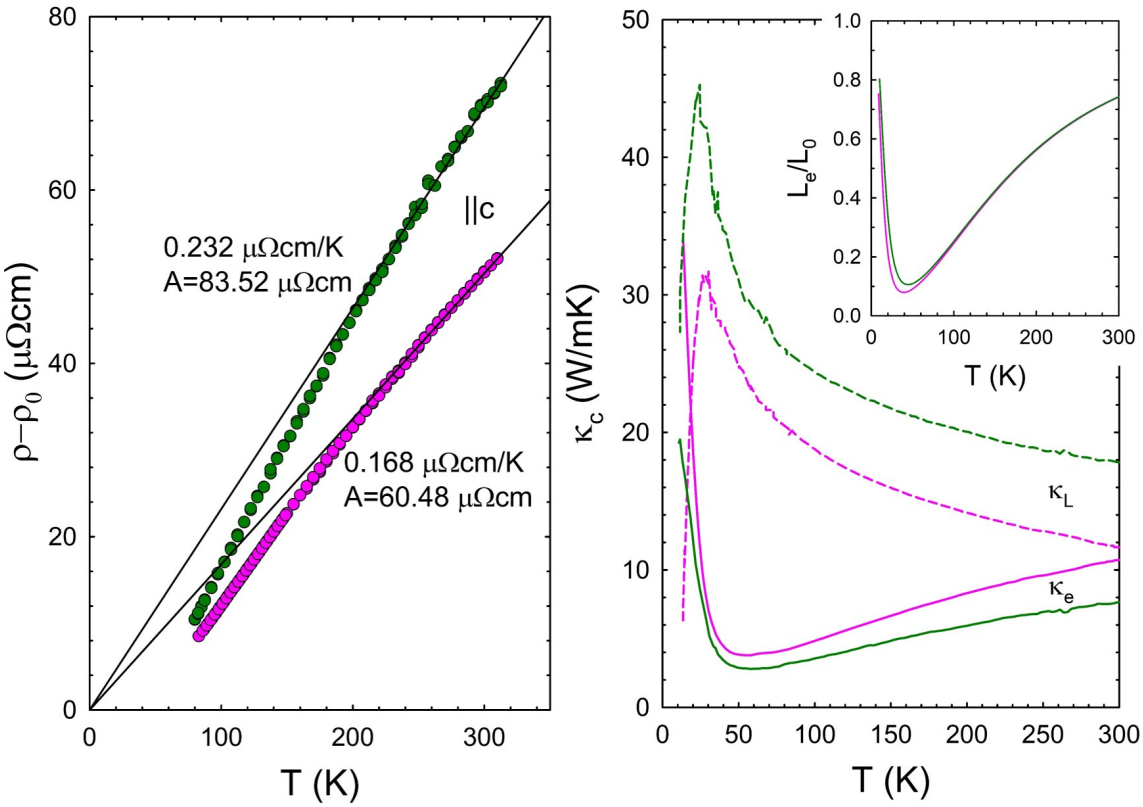


Fig. S3| Approximate separation of electronic and lattice thermal conductivities. a, High-T linear fits to the intrinsic resistivities for the two c-axis crystals from Fig. 1 used to infer the impurity parameter A (see text). **b,** Approximate electron and lattice thermal conductivities from the analysis described in the text; the computed Lorenz ratios are shown in the inset.

TABLE S2| Lorenz number analysis

Crystal	ρ_0 ($\mu\Omega$cm)	A ($\mu\Omega$cm)	$\rho_0/4A$
Crystal 1 (pink)	0.372	60.48	0.0015
Crystal 2 (green)	0.975	83.52	0.0029

$$\chi(T/\Theta, N_a) = \left(\frac{T}{\Theta}\right)^5 \left\{ \mathscr{J}_5 \left[1 + \frac{3(2N_a^2)^{1/3}}{2\pi^2} \left(\frac{\Theta}{T}\right)^2 \right] - \frac{1}{2\pi^2} \mathscr{J}_7 \right\},$$

$$\mathscr{J}_n = \int_0^{\Theta/T} \frac{z^n}{(e^z - 1)(1 - e^{-z})}\, dz,$$

where N_a is the number of conduction electrons per atom ($N_a = 1$ for Nb_3S_4).

$\kappa_e(T)$ and $\kappa_L(T)$ computed from this analysis are plotted in Fig. S3 b; the ratios L_e/L_0 for each crystal are shown in the inset. At the lowest temperatures ($T \lesssim 10$ K), $\kappa \approx \kappa_e$. Values for ρ_0 and A are listed in Table S2.

S4. Transverse Peltier conductivity and transport coefficients in the rotated coordinate system

The Peltier conductivity tensor can be expressed as,

$$\widehat{\alpha} = \widehat{\sigma}\widehat{S} = \begin{pmatrix} \sigma_{xx} & \sigma_{xy} \\ \sigma_{yx} & \sigma_{yy} \end{pmatrix} \begin{pmatrix} S_{xx} & S_{xy} \\ S_{yx} & S_{yy} \end{pmatrix} \tag{S1}$$

where $\widehat{\sigma}$ and $\widehat{S}$ are the electrical conductivity and Seebeck tensors. The off-diagonal term (transverse Peltier conductivity) which induces a transverse current $J_y = \alpha_{yx}(-\nabla_x T)$ is then given as $\alpha_{yx} = \sigma_{yx}S_{xx} + \sigma_{yy}S_{yx}$.

Any of the transport coefficients can be expressed within the x-y coordinate system in terms of the coefficients along and perpendicular to the c axis as,

$$\widehat{T} = \begin{pmatrix} T_{\perp c}\cos^2\phi + T_{\parallel c}\sin^2\phi & (T_{\perp c} - T_{\parallel c})\sin\phi\cos\phi \\ (T_{\perp c} - T_{\parallel c})\sin\phi\cos\phi & T_{\perp c}\sin^2\phi + T_{\parallel c}\cos^2\phi \end{pmatrix}$$

where $\widehat{T} = \widehat{\sigma}$, $\widehat{S}$, $\widehat{\kappa}$, $\widehat{\rho}$ etc.

S5. Tables for references to data in Fig. 2 a-c, axial power factors, S_{yx} measurement

TABLE S3| References for curves included in Fig. 2 a for Ta_2PdSe_6 [4], Yb_3Si_5 [5], $YbAl_3$ [6], $YbAgCu_4$ [7], $Na_{0.88}CoO_2$ [8], Bi_2Te_3 [9], and $TaSiTe_4$ [10].

Material	Reference
Ta_2PdSe_6	A. Nakano *et al.*, J. Phys. Energy **3**, 044004 (2021)
Yb_3Si_5	K. Kuga *et al.*, Appl. Phys. Lett. **123**, 202201 (2023).
$YbAl_3$	D. M. Rowe *et al.*, J. Phys. D: Appl. Phys. **35** 2183 (2002).
$YbAgCu_4$	P. C. Patel *et al.*, ACS Appl Energy Maters. **6**, 5037-5046 (2023).
$Na_{0.88}CoO_2$	M. Lee *et al.*, Nature Mater. **5**, 537 (2006).
Bi_2Te_3	Y. S. Hor *et al.*, J. Phys.: Condens. Matter **22** 375801 (2010).
$TaSiTe_4$	T. Inohara *et al.*, Appl. Phys. Lett. **110**, 183901 (2017).

TABLE S4| References for curves included in Figs. 2 b,c for WSi_2 [11], $MoSi_2$ [12], $LaPt_2B$ [13], MnBi [14], $UCo_{0.8}Ru_{0.2}Al$ [15], $YbMnBi_2$ [16], Fe_3Ga [17], Co_2MnGa [18], Re_4Si_7 [19], and $LuCo_6Ge_6$ [20].

Material	Reference
WSi_2	S. Ohsumi *et al.*, PRX ENERGY **3**, 043007 (2024).
$MoSi_2$	H. Manako *et al.*, Commun. Mater. **7**, 41 (2026).
$LaPt_2B$	H. Manako *et al.*, Nature Commun **15**, 3907 (2024).
MnBi	B. He *et al.*, Joule **5** 3057–3067 (2021)
$UCo_{0.8}Ru_{0.2}Al$	T. Asaba *et al.*, Sci. Adv. **7**, eabf1467 (2021).
$YbMnBi_2$	Yu Pan *et al.*, Nat. Mater. **21**, 203-209 (2022).
Fe_3Ga	A. Sakai *et al.*, Nature **581**, 53–57 (2020).
Co_2MnGa	A. Sakai *et al.*, Nat. Phys. **14**, 1119-1124 (2018).
Re_4Si_7	M. R. Scudder *et al.*, Energy Environ. Sci. **14**, 4009-4017 (2021).
$LuCo_6Ge_6$	Hu, H. *et al.*, Nat. Mater. (2026). https://doi.org/10.1038/s41563-026-02678-4.

The axial power factors, $PF = S^2/\rho$, for the same two crystals for each direction from Fig. 1, are shown in Fig. S4. Figure S5 shows the measured ΔT_x, ΔT_y and ΔV_y used to determine $S_{yx}(T)$ shown in Fig. 2e.

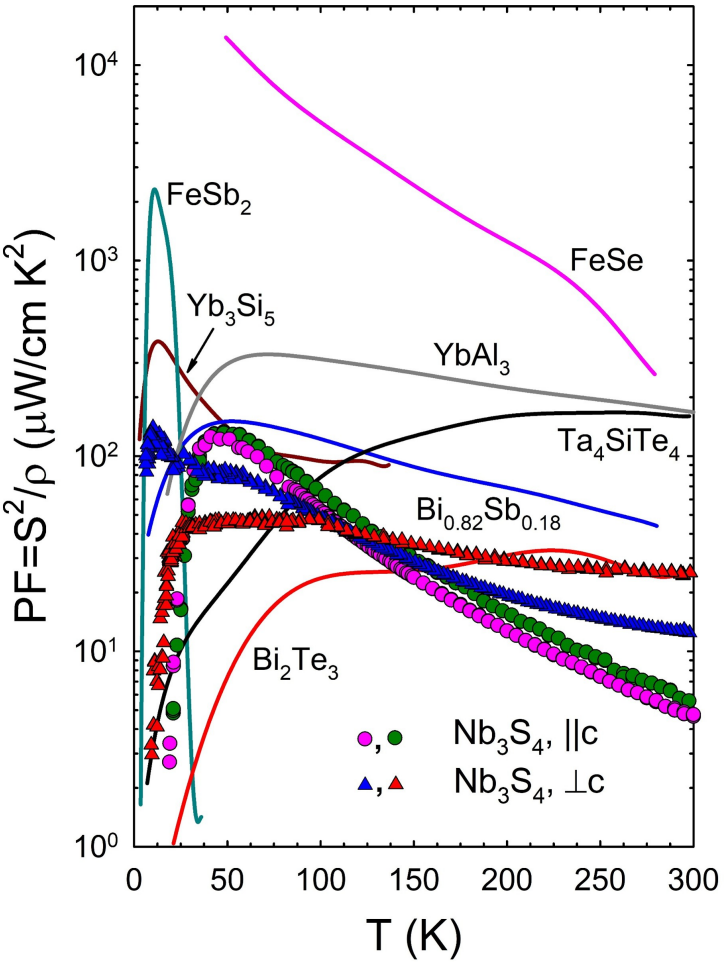


Fig. S4| Axial power factors. Axial power factors for Nb_3S_4 (symbols are the same as those from Fig. 1) compared to those of several materials from Fig. 2a and Table S2 along with those for $FeSb_2$ (Ref. 21), FeSe (Ref. 22), and $Bi_{0.82}Sb_{0.18}$ (Ref. 23).

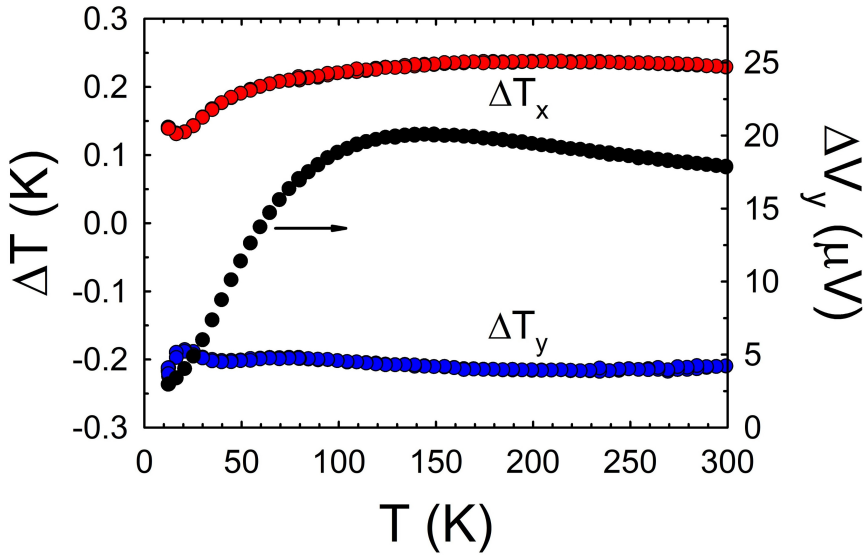


Fig. S5| Direct measurements to determine S_{yx} in Fig. 3f. Measured ΔT_x, ΔT_y, and ΔV_y (right ordinate) used to determine S_{yx} for heat flow at 45° to the cystal axes in Fig. 2f.

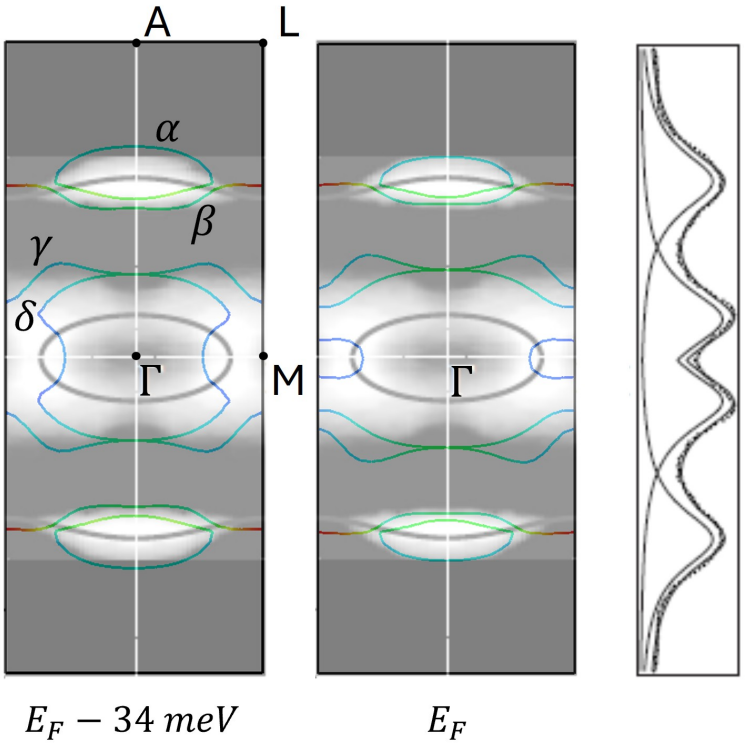


Fig. S6| Comparison of calculated and measured Fermi surfaces. Projection of the computed Fermi surface in the $\Gamma-A-L-M$ plane for Nb_3S_4 at two values of E_F (thin colored curves), overlaid on the gray-scale photoemission results from Ref. 24. The rightmost panel shows the corresponding photoemission intensity deconvolved into Lorentzians. Solid gray curves in the gray-scale projections represent the local maxima of intensity from Ref. 24.

S6. Comparison of DFT FS to experiment

Figure S6 shows the projection of the computed Fermi surface (FS) in the $\Gamma-A-L-M$ plane for Nb_3S_4 at different values of E_F, overlaid on the photoemission intensity map from Ref. 24. Overall our calculations approximate the photoemission well, though the intensity maxima occur at somewhat smaller k_z momenta than the computed crossings for bands γ and δ. Also note that it was inferred in Ref. 24 that the inner Fermi surface (designated here as δ) is closed along the $\Gamma-M$ direction as indicated by the thick gray ellipse reflecting the locus of maximum intensity. In our calculations the δ Fermi surface is only closed for E_F shifted ~ 34 meV lower than the DFT value (left panel, Fig. S6). At the DFT value for E_F (right panel), the δ-band FS doesn't reach the zone boundary along $\Gamma-M$ in a narrow k_z momentum range (defined by the dark blue contour centered at the M point). This finite extent may be interpreted to be responsible for the intensity maximum in photoemission along $\Gamma-M$.

S7. Orbital character of the FS sheets and extent of the ADCP character within the CRTA

The orbital character of each of the four FS sheets is depicted [24] in Fig. S7. Also shown is the orbital character of the δ band in the extended van-Hove singularity region of phase space responsible for the sharp density of states peak near 10.2 meV.

The extent of the calculated ADCP behavior predicted within the CRTA was assessed by shifting E_F from the DFT value and calculating the thermopowers assuming rigid bands – these results are shown in Fig. S8 as $S_{\perp c} - S_{|c}$ versus the Fermi-level shift, ΔE_F, at three temperatures.

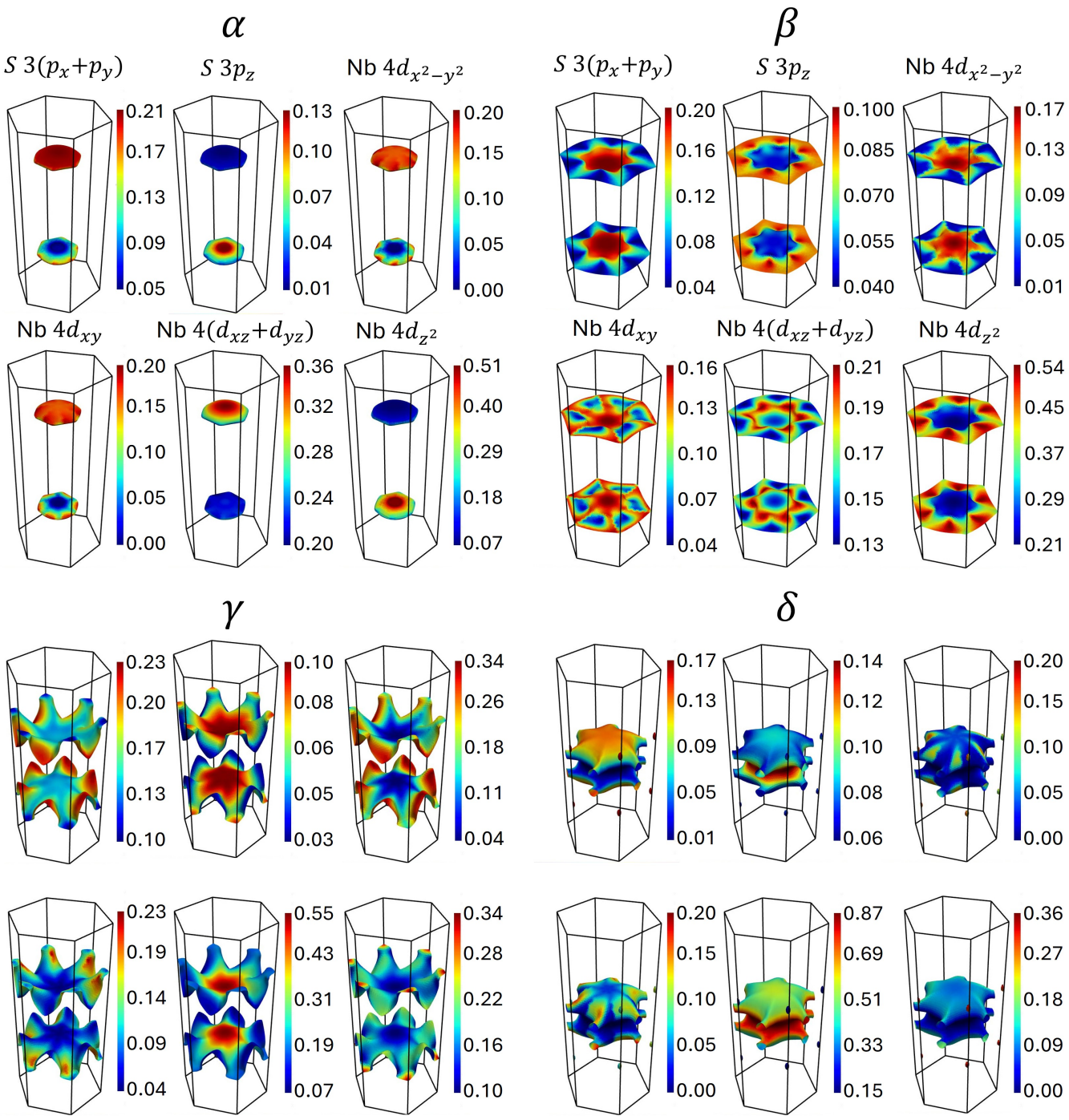


Fig. S7| Orbital character of the FS sheets. Color maps depicting the orbital character of the four FS sheets ($\alpha - \delta$). Color scales indicate the fraction for each orbital represented.

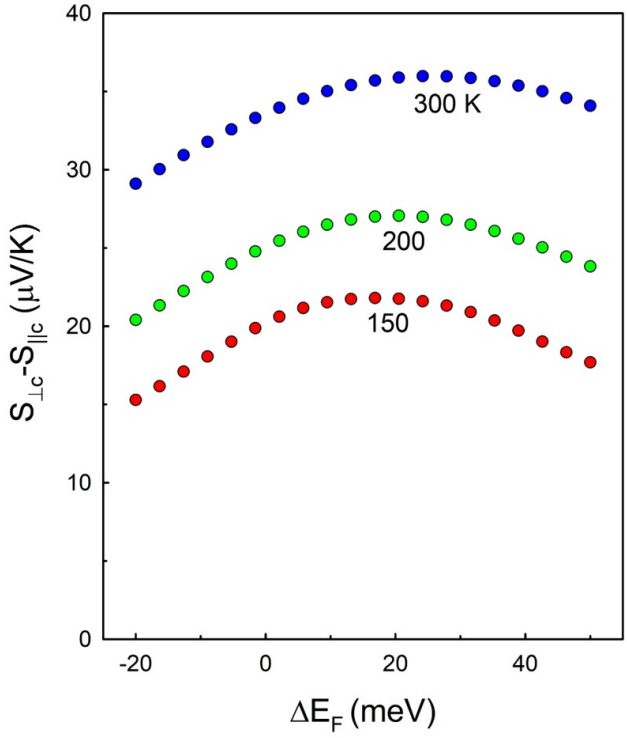


Fig. S8| Range of the computed ADCP behavior for rigid-band shifted E_F. The computed difference in axial thermopowers, $S_{\perp c} - S_{\|c}$, as functions of the rigid-band-shifted Fermi energy (from the DFT value) at three temperatures.

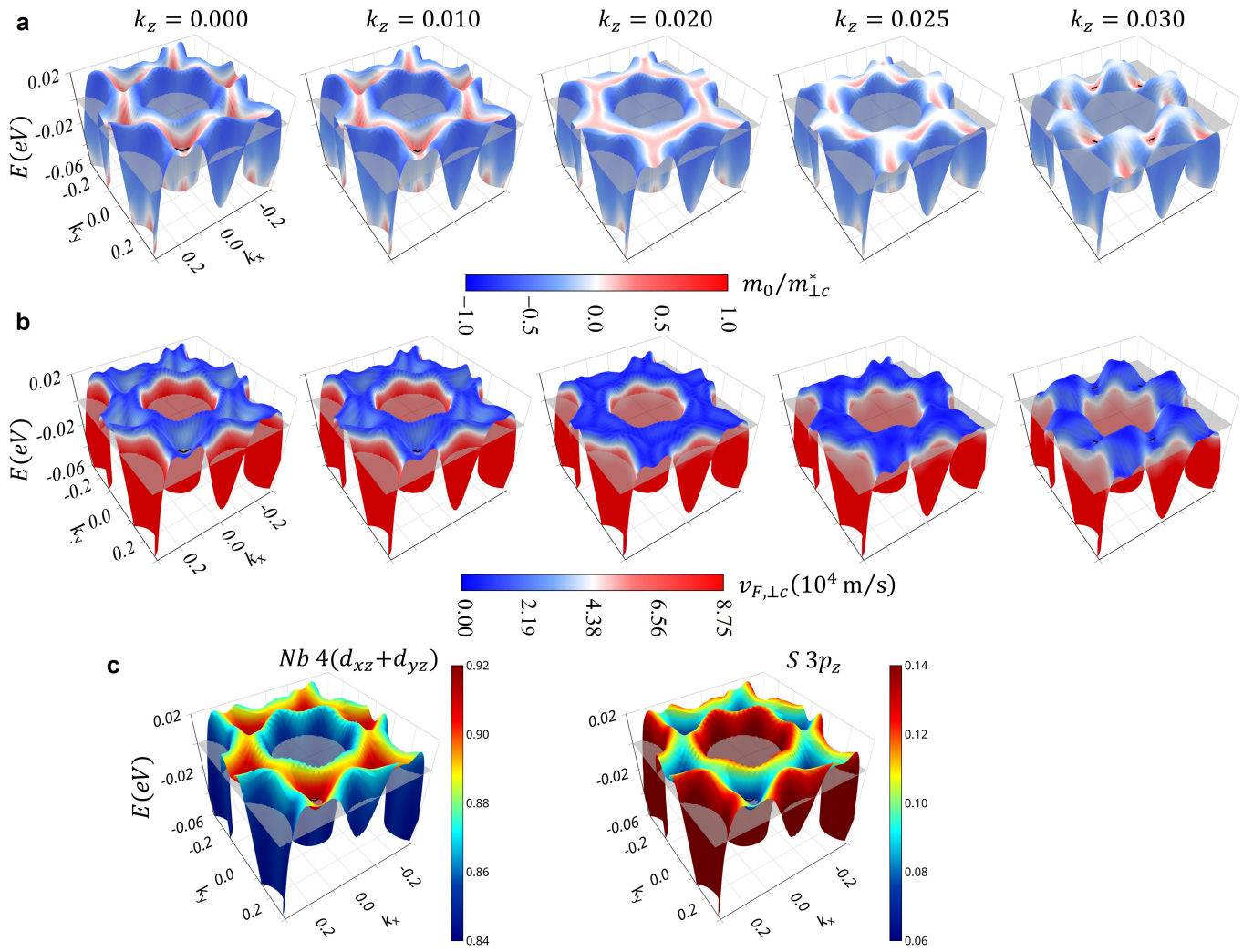


Fig. S9| Mapping the nearly-localized states of the δ band responsible for the density of states peak near E_F. 3D contour plots of the in-plane dispersions for band δ with color maps of the inverse effective masses (**a**) and in-plane Fermi velocities (**b**) for various c-axis momenta k_z (in $2\pi/c$ units) showing the the region of nearly-localized states associated with the extended van Hove singularity (see also Fig. 3l). The k_x and k_y units are Bohr^{-1}. **c**, Fractional orbital composition of the states (for $k_z = 0$).

S8. Further characterization of the extended van Hove singularity and nearly-localized states

Figure S9 shows 3D contour plots of the in-plane dispersions for band δ with color maps of the inverse effective masses (a) and in-plane velocities, $v_{F,\perp c}$ (b), at various k_z momenta near the van Hove singularity underlying the sharp peak in the density of states at 10.2 meV. The dispersions are particularly flat for $k_z \lesssim 0.025$, as more clearly seen in the line plots of Fig. S10a, c. We can estimate the fraction of the BZ volume represented by these states using the area between the circle of radius $k_\perp$ (defined in Fig. 3l) and the BZ boundary (the hatched region depicted in Fig. S10d) to be $f = [1-(\pi k_\perp^2/A_{hex})][\Delta k_z/(\pi/c)] \simeq 0.022$ (or 2.2%), where $A_{hex} = (6/\sqrt{3})b^2$, $k_\perp = \pi(0.78b)^2$, $\Delta k_z = 0.025(2\pi/c)$, and $b = [2/(3\sqrt{3})](\pi/a)$ is the $\Gamma - M$ distance. The constraint, from Fig. S10c, restricts the volume estimate to states for which $v_{F,\perp} \lesssim 2\times 10^4$m/s.

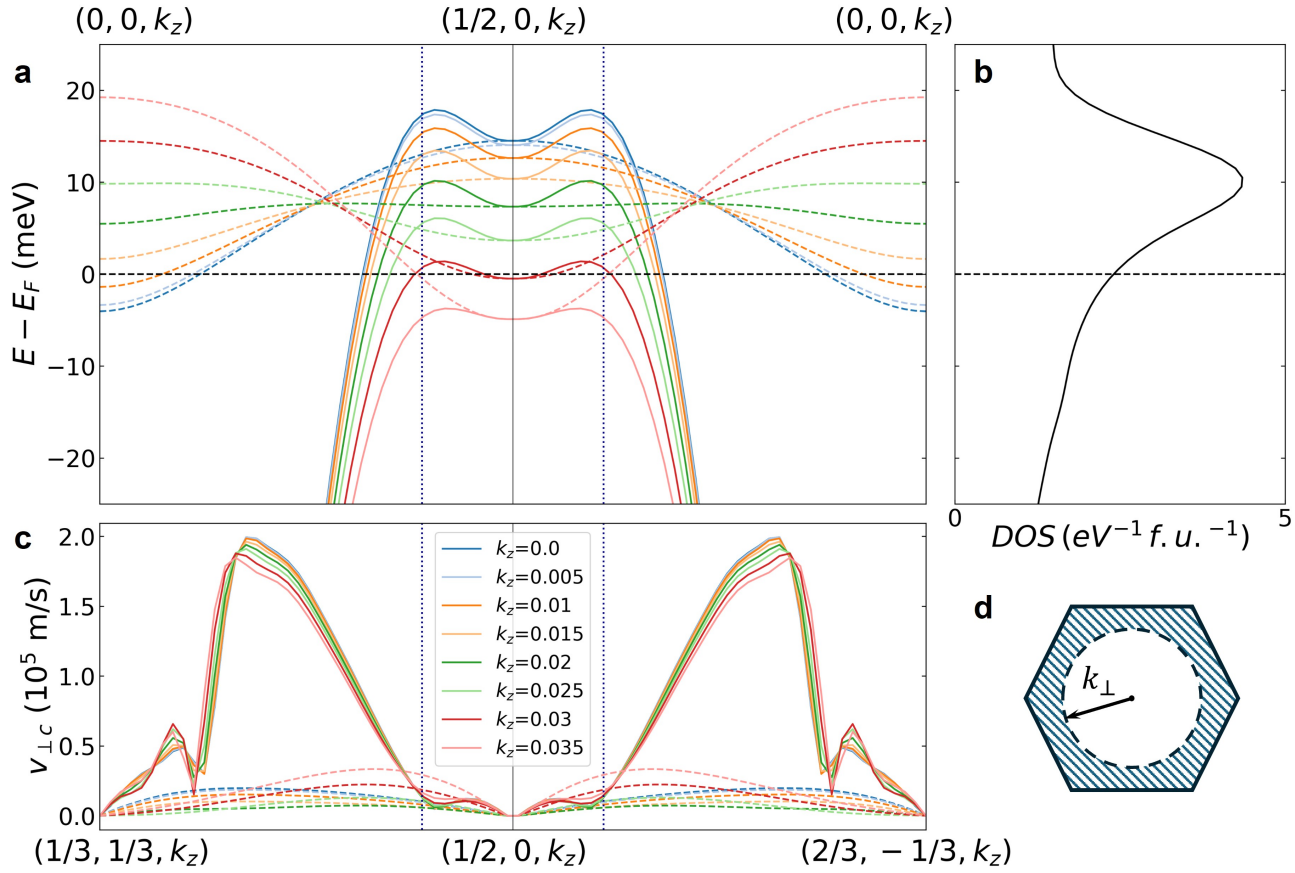


Fig. S10| Evolution with k_z of the extended van Hove singularity. **a**, Band-δ dispersions along the $\Gamma - M - \Gamma'$ (solid) and $K - M - K'$ (dashed) directions at various k_z showing a flattening saddle point at M. Solid (dashed) curves refer to the upper (lower) abcissa. **b**, DOS for the δ band. **c**, The corresponding group velocities; blue vertical cutoff lines define the momentum region of nearly-localized states. **d**, Scheme used to estimate the in-plane BZ area of the nearly-localized states (hatched region).

S9. Modeling a scattering rate inversely proportional to the electronic density of states

To assess the approximate magnitude of the logarithmic energy derivative of a scattering time proportional to the δ band's inverse density of nearly-localized states (see main text and Fig. 3l), we first fitted the density of states to a sum of a Lorentzian, $L(E) = a\Gamma/((E-E_0)^2+\Gamma^2)$, and piecewise linear or constant terms to represent the asymmetric background (Fig. S11 a). The Lorentzian parameters were $a = 0.0195$, $E_0 = 10.2$ meV and $\Gamma = 6.3$ meV. Model scattering rates were taken to be a sum of a constant ($\tau_0 = 10^{14}\text{s}^{-1}$) and a rate $BL(E)$, where B is a constant dictating the strength of the energy-dependent scattering (Fig. S11b), i.e. $\tau = \tau_0/[1+BL(E)]$.

The logarithmic energy derivatives of the modeled τ evaluated at E_F (inset, S11b) appear in the Mott expression and are compared to the band structure terms $L'_{\perp c}/L_{\perp c}(L'_{\parallel c}/L_{\parallel c})|_{\varepsilon_F}$ for each band and direction in Table S5. Even for the smaller weightings of the Lorentzian, $B = 0.05, 0.2$, which suppress τ by 13% and 38% at $E = E_0$, respectively (Fig. S11b), we see that the scattering term is comparable in magnitude to or larger than the band structure terms, and thus considerably enhances the magnitudes of the $S_{\perp c}$ values and is sufficient even at $B = 0.05$ to reverse the sign of all negative values for $S_{\parallel c}$. Anisotropy in the phonon coupling of the dispersive states for each band to the nearly-localized states is anticipated and thus variations in suitable values of B by band and direction are plausible.

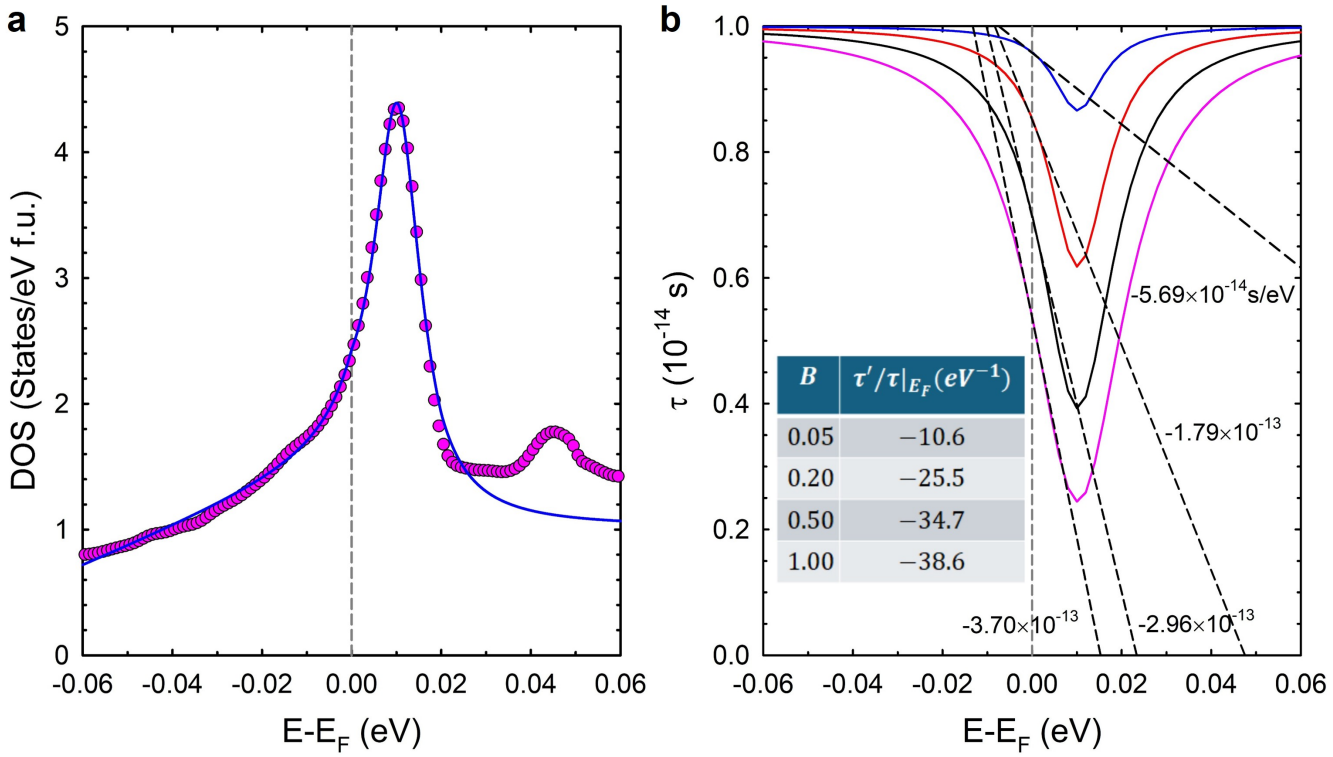


Fig. S11| Modeling energy-dependent scattering associated with the localized states. a, The δ-band density of states (circles) and an approximate fit using piece-wise linear or constant terms added to a Lorentzian ($L(E)$), **b**, Model scattering times that are the inverse of a sum of a constant rate ($\tau_0^{-1} = 10^{14}\text{s}^{-1}$) and a rate proportional to the Lorentzian employed in **a**, $BL(E)$, where B is a constant. Black dashed lines are linear least-squares fits used to determine $\tau'(E)|_{E_F}$ (with values labeling each fit). The inset shows the corresponding values for the logarithmic derivative $\tau'(E)/\tau(E)|_{E_F}$ for each value of B.

TABLE S5| Logarithmic energy derivatives of the axial transport distribution functions, evaluated at E_F, for each band, and corresponding thermopowers at $T = 300$ K computed from the Mott expression without no scattering term ($B = 0$) and with scattering strengths $B = 0.2, 0.05$ (inset Fig. S11 b.)

Band	$L'_{\perp c}/L_{\perp c}(L'_{\parallel c}/L_{\parallel c})\|_{\varepsilon_F}$ (eV^{-1})	$S^{B=0}_{\perp c}(S^{B=0}_{\parallel c})$ (μV/K)	$S^{B=0.2}_{\perp c}(S^{B=0.2}_{\parallel c})$ (μV/K)	$S^{B=0.05}_{\perp c}(S^{B=0.05}_{\parallel c})$ (μV/K)
α	-22.9 (-17.9)	168 (131)	355 (318)	246 (209)
β	-16.8 (3.22)	123 (-23.6)	310 (163)	201 (54.1)
γ	-5.38 (4.46)	39.5 (-32.7)	227 (154)	117 (45.0)
δ	1.39 (9.10)	-10.2 (-66.7)	177 (120)	67.6 (11.0)

S10. T^3 behavior of resistivities

Figure S12 shows intrinsic resistivity $\rho_i(T) \equiv \rho(T) - \rho_0$ for the four crystals from Fig. 1 of the main text on a log-log scaling, demonstrating $\rho_i(T) \propto T^n$ behavior with $n \simeq 3$. As noted in the main text, this is a signature of interband scattering [26, 27], typical of transition metals with overlapping bands of highly-dispersive and nearly-localized states. An alternate explanation for this behavior was proposed for the Nb_3X_4 (X=S, Se, Te) compounds [14, 21] to originate, for transport $\|c$, from electron-electron Umklapp scattering by two electrons between the q1D outer Fermi surface sheets (band γ) [25], the combined momentum transfer for which corresponds the reciprocal lattice vector $\pm 2\pi/c$. As T exceeds the characteristic warping of the FS sheets, the phase space for this scattering should grow, leading to a higher power for the Umklapp scattering than the typical T^2.

We can expect a freeze-out of interband transitions from the most dispersive states responsible for conduction to the nearly-localized states when T becomes lower than the characteristic temperature, $T^* \simeq \hbar\omega/(2.82k_B)$, at which the phonon energy $\hbar\omega$ is dominant in the Bose distribution *and* corresponds to the minimum wavenumber bridging the initial and final states. Figure S13 shows the computed phonon spectrum with the relevant energy range shaded. For conduction $\|c$,

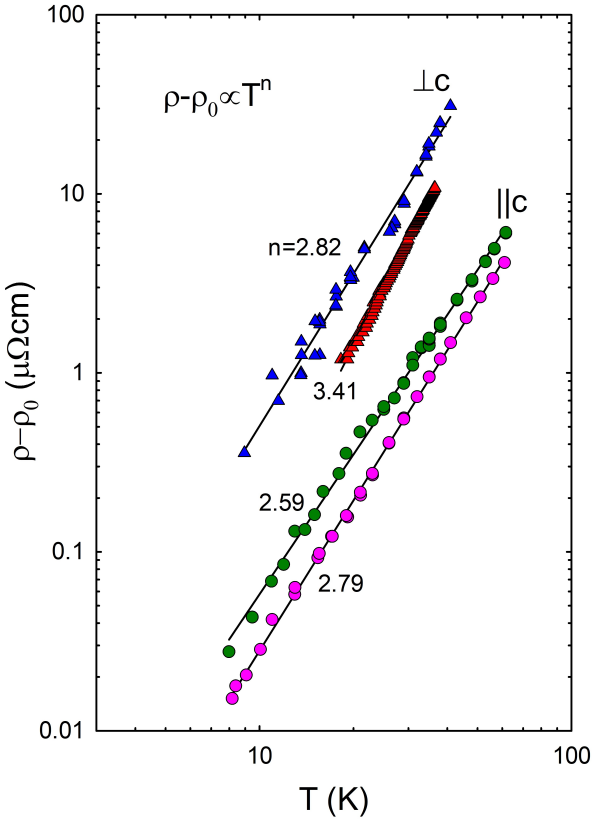


Fig. S12| $T^n (n \simeq 3)$ **behavior of the resistivities.** The intrinsic resistivities $\rho_i(T) \equiv \rho(T) - \rho_0$ versus T for the crystals from Fig. 2 of the main text.

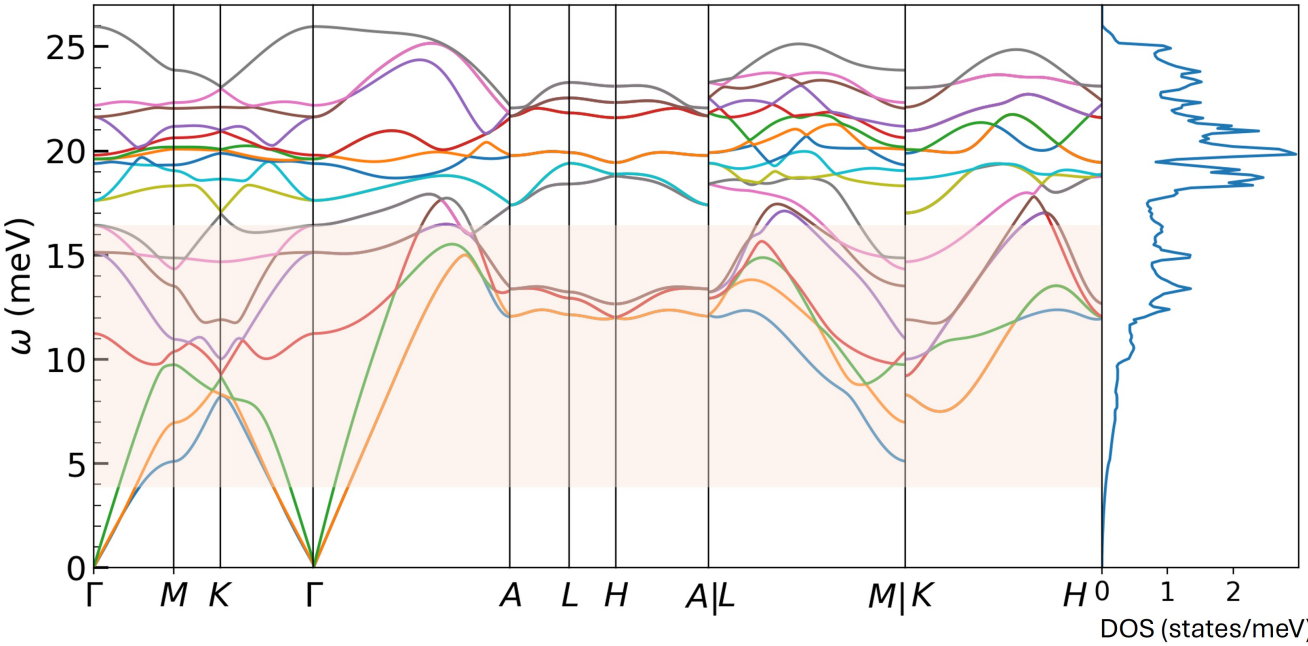


Fig. S13| **Phonon dispersions and density of states.** Computed phonon band dispersions along high-symmetry directions and phonon density of states for Nb_3S_4. The shaded region corresponds to the energy range of the nearly-localized states of the δ band (see Figs. S10 and S11 a).

the minimum wavenumber for the most dispersive states of the β sheet is $q_z \simeq \pi/2c$. Phonons having this q_z correspond to energies of 10-15 meV, thus we expect their numbers to decline (using 12.5 meV) starting at $T^* \simeq 52$ K. The γ sheet, predominant for conduction $\perp c$, requires smaller minimum q values and thus we anticipate a lower temperature for the freeze-out, with $T^* \simeq 20$ K for the minimum 4.9 meV phonons. These temperatures agree well with the range of the experimental T^3 behavior.

S11. Phonon dispersions and density of states

Phonon dispersions and densities of states were computed within the framework of density functional perturbation theory as implemented in Quantum ESPRESSO, using the self-consistent charge density obtained on a Monkhorst-Pack k-point mesh of $8 \times 8 \times 20$ with kinetic energy cutoffs of 100 Ry and 600 Ry for the plane-wave basis set and charge density, respectively. Dynamical matrices were evaluated on a $3 \times 3 \times 8$ q-point mesh, with a phonon self-consistency threshold of 10^{-14} imposed to ensure fully converged force constants, from which phonon dispersions and vibrational densities of states were obtained by Fourier interpolation. The phonon dispersions for $Nb3S_4$ are shown in Fig. S13.

[1] Cullity, B. D. & Stock, S. R. *Elements of X-ray Diffraction*, 3rd ed. (Prentice Hall, Upper Saddle River, NJ, 2001).
[2] Makinson, R. E. B. The thermal conductivity of metals, *Math. Proc. Cambridge Phil. Soc.* **34**, 474-497 (1938).
[3] We employed an average of the Θ values reported in Refs. 17, 18.
[4] Nakano, A., Yamakage, A., Maruoka, U., Taniguchi, H., Yasui, Y. & Terasaki, I. Giant Peltier conductivity in an uncompensated semimetal Ta_2PdSe_6. *J. Phys. Energy* **3**, 044004 (2021).
[5] Kuga, K., Hirata, K., Matsunami, M. & Takeuchi, T. Huge Peltier conductivity in valence fluctuating material Yb_3Si_5. *Appl. Phys. Lett.* **123**, 202201 (2023).
[6] Rowe, D. M., Kuznetsov, V. L., Kuznetsova, L. A., & Min, G. Electrical and thermal transport properties of intermediate-valence $YbAl_3$. *J. Phys. D: Appl. Phys.* **35**, 2183 (2002).
[7] Koirala, M., Wang, H., Pokharel, M., Lan, Y., Guo, C., Opeil, C. & Ren, Z. Nanostructured $YbAgCu_4$ for Potentially Cryogenic Thermoelectric Cooling. *Nano Lett.* **14**, 5016 (2014).
[8] Lee, M., Viciu, L., Li, L., Wang, Y., Foo, M. L., Watauchi, S., Pascal Jr, R. A., Cava, R. J. & Ong, N. P. Large enhancement of the thermopower in Na_xCoO_2 at high Na doping, *Nat. Mater.* **5**, 537 (2006).
[9] Hor, Y. S., Qu, D., Ong, N. P. & Cava, R. J. Low temperature magnetothermoelectric effect and magnetoresistance in Te vapor annealed Bi_2Te_3, *J. Phys.: Condens. Matter* **22**, 375801 (2010).
[10] Inohara, T., Okamoto, Y., Yamakawa, Y., Yamakage, A. & Takenaka, K. *Appl. Phys. Lett.* **110**, 183901 (2017).
[11] Ohsumi, S., Sato, Y. J. & Okazaki, R. Transverse thermoelectric conversion in the mixed-dimensional semimetal WSi_2. *PRX ENERGY* **3**, 043007 (2024).
[12] Manako, H., Ohsumi, S., Yoshida, S., Okazaki, R. & Sato, Y. J. Axis-dependent conduction polarity and transverse thermoelectric conversion in the mixed-dimensional semimetal $MoSi_2$. *Commun. Mater.* **7**, 41 (2026).
[13] Manako, H., Ohsumi, S., Sato, Y. J., Okazaki, R. & Aoki, D. *Nat. Commun.* **15**, 3907 (2024).
[14] He, B. Şahin, C., Boona, S. R., Sales, B. C., Pan, Y., Felser, C., Flatté, M. E. & Heremans, J. P. Large magnon-induced anomalous Nernst conductivity in single-crystal MnBi. *Joule* **5** 3057–3067 (2021)
[15] Asaba, T., Ivanov, V., Thomas, S. M., Savrasov, S. Y., Thompson, J. D., Bauer, E. D. & Ronning, F. Colossal anomalous Nernst effect in a correlated noncentrosymmetric kagome ferromagnet. *Sci. Adv.* **7**, eabf1467 (2021).
[16] Pan, Y., Le, C., He, B., Watzman, S. J., Yao, M., Gooth, J., Heremans, J. P., Sun, Y. & Felser, C. Giant anomalous Nernst signal in the antiferromagnet $YbMnBi_2$. *Nat. Mater.* **21**, 203-209 (2022).
[17] Sakai, A. *et al.*, Iron-based binary ferromagnets for transverse thermoelectric conversion. *Nature* **581**, 53–57 (2020).
[18] Sakai, A. *et al.*, Giant anomalous Nernst effect and quantumcritical scaling in a ferromagnetic semimetal. *Nat. Phys.* **14**, 1119-1124 (2018).
[19] Scudder, M. R., He, B., Wang, Y., Rai, A., Cahill, D. G., Windl, W., Heremans, J. P. & Goldberger, J. E. Highly efficient transverse thermoelectric devices with Re_4Si_7 crystals. *Energy Environ. Sci.* **14**, 4009-4017 (2021).
[20] Hu, H. *et al.*, Fermiology-driven goniopolar transverse thermoelectricity in kagome metals. *Nat. Mater.* (2026). https://doi.org/10.1038/s41563-026-02678-4.
[21] Takahashi, H., Okazaki, R., Ishiwata, S., Taniguchi, H., Okutani, A., Hagiwara, M. & Terasaki, I. Colossal Seebeck effect enhanced by quasi-ballistic phonons dragging massive electrons in $FeSb_2$, *Nat. Commun.* **7**, 12732 (2016).
[22] Shimizu, S., Shiogai, J., Takemori, N., Sakai, S., Ikeda, H., Arita, R., Nojima, T., Tsukazaki, A., & Iwasa, Y., Giant thermoelectric power factor in ultrathin FeSe superconductor, *Nat. Commun.* **10**, 825 (2019).
[23] Lenoir, B., Dauscher, A., Cassart, M., Ravich, Yu., & Scherrer, H. Effect of Antimony Content on the Thermoelectric Figure of Merit of $Bi_{1-x}Sb_x$ Alloys, *J. Phys. Chem So1.* **59**, 129 (1998).
[24] Herath, U., Tavadze, P., He, X., Bousquet, E., Singh, S., Muñoz, F. & Romero, A. H. PyProcar: A Python library for electronic structure pre/post-processing. *Comp. Phys. Commun.* **251**, 107080 (2020).

[25] Oshiyama, A., Nakao, K. & Kamimura, H. Electrical Resistivity due to Electron-Electron Scattering in Quasi-One-Dimensional Metals. *J. Phys. Soc. Jpn.* **45**, 1136-1146 (1978).